Breaking of the Phosphodiester Bond: A Key Factor That Induces Hemolysis

Tiantian Wang[†,‡] and Xiue Jiang*[,†]

[†]State Key Laboratory of Electroanalytical Chemistry, Changchun Institute of Applied Chemistry, Chinese Academy of Sciences, Changchun 130022, China

[‡]Graduate University of Chinese Academy of Sciences, Beijing 100049, China

S *Supporting Information*

ABSTRACT: In-depth understanding the toxicity of nanomaterials in red blood cells (RBCs) is of great interest, because of the importance of RBCs in transporting oxygen in blood circulation. Although the toxic effects of nanoparticles in RBCs have been revealed, the conclusions from the literature are conflicting, and in particular, the toxic mechanism is still at the infant stage. Herein, we investigated the size-dependent toxicity of well-known CdTe semiconductor quantum dots (QDs) and revealed the exact toxic mechanism at the molecular level by confocal microscopy and Fourier transform infrared (FT-IR) spectroscopy techniques. We found that smaller mercaptosuccinic acid-capped CdTe QDs (MSA-QDs) with the green-emitting color could cause hemagglutination whereas the middle-size yellow-emitting MSA-QDs induced the formation of stomatocytes and echinocytes and the bigger size red-emitting MSA-QDs induced heavy hemolysis and the formation of lots of ghost cells. The FT-IR data proved that all the MSA-QDs were likely to bond to the RBCs membranes and caused the structural changes of lipid and protein in RBCs. But only the red-emitting MSA-QDs caused the breakage of the phosphodiester bond, which might cause the heavy hemolysis. To some extent, this is the first example that reveals the hemolysis mechanism at the molecular level.

KEYWORDS: semiconductor quantum dots, red blood cells, hemolysis mechanism, FT-IR spectroscopy, confocal microscopy, cytotoxicity
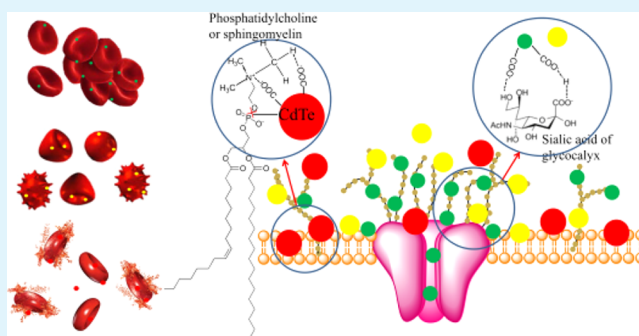
1. INTRODUCTION

With the application of nanomaterials in drug delivery systems, RBCs are often exposed to nanomaterials,[1−3] which always causes the hemolysis of RBCs. Therefore, the toxicity of nanomaterials in RBCs has been widely investigated. The factors that influence the hemolytic activity involve the particle size,[4−6] geometry,[2] concentration,[5] composition,[1] surface modifications,[5] and the surrounding environment.[6] Since the particle size is one of the key factors that decides if the particles can be recognized and cleared away by mononuclear phagocytic system, the study of size-dependent hemolysis is extremely important for the application of nanoparticles in nanomedicine. Some researchers reported that smaller nanoparticles with a larger surface area were more hemolytic than larger ones.[4−6] However, Zhao et al. found that larger nanoparticles exhibited greater hemolytic activity than smaller ones.[3] In order to study the hemolysis mechanism of nanoparticles, some researchers observed the nanoparticles-induced morphological changes of RBCs.[1,3] They found that hemolysis was induced by the damage to cell membranes, such as pores[1] and echinocytes formation.[3] Nevertheless, these conflicting results stress the need for in-depth research on the mechanism that controls the hemolysis.

The factors that control the shape of RBCs include the content of ATP[7−9] and the structure of phospholipid bilayer and spectrin in membranes.[10,11] For in-depth understanding of the hemolysis mechanism, a study of nanoparticle-induced structural changes of RBCs is necessary, in addition to the observation of morphological transformation. Unfortunately, this has been given little attention, although many researchers have studied the hemolytic activity of many types of nanomaterials.[2,4−6,12−14] FT-IR spectroscopy has been proven to be a powerful analytical method in studying the molecular conformational order of biological membranes.[15−18] Because of the great ability of FT-IR spectroscopy in detecting the global biochemical information on the intact cells, it has been successfully used in distinguishing differences among cell populations.[19−23] However, FT-IR spectroscopy has been used less in studying the nanomaterial-induced hemolytic phenomenon until now, except that we have employed surface-enhanced FT-IR spectroscopy to study the interaction of QDs

with model membranes prepared on solid supports,[24] whereas model membranes cannot truly reflect the real cells.

In addition, semiconductor QDs have been widely used in biomedical applications as probes for *in vitro*[25] and *in vivo* imaging[26] including vascular imaging.[27] The small size enables them to overcome, or even avoid, various biological barriers and invade living organisms. Therefore, there are increasing concerns with regard to the nanotoxicity of semiconductor QDs. Although the toxicity of QDs has been studied in many works,[28−31] their size-dependent hemolytic effect on RBCs has not been reported as far as we know. Here, we selected MSA-QDs as model QDs to study the size-dependent toxicity of QDs in RBCs via hemolysis testing, since the aqueous synthesis of the QDs with small ligand as stabilizer makes it easy to get various diameters. The observation of confocal microscopy revealed that the particles of different sizes would cause different changes in the shape of RBCs, and the corresponding structural changes of RBCs membranes were analyzed by FT-IR spectroscopic approach. On the basis of these correlating results, we could reveal that the breaking of the phosphodiester bond might be the key factor that induced hemolysis.

2. EXPERIMENTAL SECTION

2.1. Synthesis of Mercaptosuccinic Acid-Capped CdTe Quantum Dots (QDs) and Physicochemical Properties. The mercaptosuccinic acid-capped CdTe QDs were prepared as the reported procedures.[32,33] Briefly, 4 mL of 0.04 mol L^{-1} cadmium chloride (CdCl$_2$) aqueous solution was diluted to 50 mL in a one-necked flask, and then 100 mg of trisodium citrate dihydrate, 4 mL of 0.01 mol L^{-1} Na$_2$TeO$_3$ (Aldrich) aqueous solution, 50 mg of mercaptosuccinic acid (MSA, Aldrich), and 50 mg of sodium borohydride (NaBH$_4$) were added together into the one-necked flask under stirring. After the solution gradually changed to a yellow color, the flask was attached to a condenser and refluxed at 100 °C in open air. The green-, yellow-, and red-emitting MSA-QDs were obtained after refluxing for ~1.5, 5, and 12 h, respectively. The as-prepared MSA-QDs solution was mixed with absolute alcohol at a volume ratio of 1:3 and separated by centrifugation at 10 000 rpm for 20 min. The precipitation was evaporated in a vacuum case overnight, and dispersed in phosphate buffered saline (PBS, pH 7.4) as a stock solution and kept at 4 °C. The as-prepared MSA-QDs were characterized by a Cary 500 Scan ultraviolet−visible (UV-vis) spectrophotometer (Varian, USA) and a Fluoromax-4 spectrofluorometer (Horiba Jobin Yvon, Inc., France), respectively. The hydrodynamic sizes were characterized by fluorescence correlation spectroscopy using a home-built setup.[34] The zeta potential (ζ) was determined using a Zetasizer (ZEN3600, Malvern Co., U.K.).

2.2. Hemolysis Assay. RBCs were obtained from multiple healthy adult volunteers in the Hospital of Integrated Traditional and Western Medicine in Jilin province. Whole blood was centrifuged at 4000 rpm for 3 min to remove plasma, buffy coat, and the top layer of cells. The remaining cells were washed five times with sterile PBS. After that, 200 μL of packed RBCs were diluted to 3 mL with PBS. Then, 200 μL of the RBCs taken from the 3 mL stock solution were mixed with 800 μL of the green-, yellow-, and red-emitting MSA-QDs in PBS at a final concentration of 500 μg mL^{-1}, respectively. The negative and positive control samples were prepared by mixing 200 μL of RBCs suspension with PBS and water respectively, instead of MSA-QDs solution. The mixtures were incubated in a humidified incubator at 37 °C, 5% CO$_2$ for 3 h, and then

centrifuged at 1000 rpm for 5 min. The supernatant was used for UV-vis measurements. The percentage of the hemolytic RBCs was calculated using the following formula:

$$\text{percent hemolysis (\%)} = \frac{A_s - A_n - A_-}{A_+ - A_-} \times 100$$

where A_s is the sample absorbance and A_n is the nanoparticle absorbance; A_+ and A_- are the positive control and negative control absorbances, respectively.

2.3. Cellular Images. After the supernatant was removed for UV-vis measurements, the sediment RBCs were washed three times with PBS and resuspended in 2 mL of PBS. Then, 800 μL of the suspension was introduced into a 35-mm tissue culture dish (NEST Biotech Co., Ltd., China). After 20 min of culture at room temperature, the cells were washed with PBS and imaged by confocal laser scanning fluorescence microscope (CLSM, Leica TCS SP2, Leica Microsystems, Mannheim, Germany) with 100× objective in the bright field.

2.4. FT-IR Spectroscopy. Alternatively, after removing the supernatant and washing three times, 10 μL of the sediment RBCs were spread uniformly on the surface of an attenuated total reflectance (ATR) accessory with a silicon crystal. Cells were then dried at room temperature under airflow for 20 min. All ATR−FT-IR absorption spectra were recorded with a spectrometer (IFS 66v/s, Bruker, Ettlingen, Germany) equipped with a liquid-nitrogen-cooled MCT detector. For each spectrum, 256 scans were collected with a spectrum resolution of 4 cm^{-1}. The spectrum was corrected by subtraction of absorption band of vaporized water in the atmosphere. In order to enhance spectral resolution, some spectra were decomposed by Gaussian curve-fitting analysis using the OPUS 5.0 software. The positions of the component bands determined by the second-derivative peaks were set as the initial input parameters, and the program iterated to achieve the best Gaussian-shaped curves. The relative amounts of different compositions were calculated from the integrated areas of the component bands.

The experimental setup for surface-enhanced FT-IR spectroscopy and procedures for preparing Au film as enhanced substrate have been described elsewhere.[35−37] After Au film preparation, the Au film was immersed in 1 mM 1-dodecanethiol (DT, Sigma−Aldrich) dissolved in ethanol for 1 h, and the signal was recorded with pure ethanol as reference. After the substrate was sequentially washed with ethanol and double-distilled water three times, 200 μL of double-distilled water was added for the reference measurement. A sample spectrum was measured after 750 μL of vesicle solution was added for 3 h. After the substrate was washed sufficiently with water, a reference spectrum was recorded upon the addition of 300 μL of water. Then, a sample spectrum was recorded after 100 μg mL^{-1} of MSA-QDs aqueous solution was incubated with model lipid for 3 h. As contrast experiment, we also measured the spectra of MSA-QDs after 100 μg mL^{-1} of MSA-QDs aqueous solution was added to Au film for 3 h with water as reference.

2.5. Preparation of Lipid Vesicles. The supported lipid bilayer membranes were prepared as the method described previously.[24] Egg phosphatidylcholine (egg PC), sphingomyelin (SM), dioleoylphosphoethanolamine (DOPE), dioleoylphosphatidylserine (DOPS), and cholesterol (Sigma−Aldrich, St. Louis, MO) were mixed in ratios of 1:1:1:1:2 (by weight). The mixtures were suspended in chloroform, and the solvent was

removed in a N$_2$ stream to initiate the formation of a thin lipid layer, followed by the treatment in a vacuum chamber for 30 min for removing the solvent thoroughly. Double-distilled water was added to yield a final concentration of 1.5 mg mL^{-1}. Sonication (Kunsan Instrument, Jiangsu, China) at 40 °C for 1 h yielded a clear solution. The vesicles were always used within 24 h after preparation.

3. RESULTS AND DISCUSSION

3.1. Size-Dependent MSA-QDs Hemocompatibility. In order to investigate the size-dependent hemolytic activity, we synthesized green-, yellow-, and red-emitting MSA-QDs with diameters of 2.3, 3.5, and 5.4 nm, respectively, and nearly the identical zeta potential. The physicochemical properties of these nanoparticles are compiled in Table 1. To evaluate the

Table 1. Physicochemical Properties of MSA-QDs

quantum dot	λ_{abs} (nm)[a]	λ_{em} (nm)[b]	ζ-potential (mV)	diameter (nm)
red	595	624	−18.58 ± 1.02	5.4 ± 0.2
yellow	544	568	−22.48 ± 0.78	3.5 ± 0.3
green	530	549	−22.72 ± 2.23	2.3 ± 0.2

[a]Typical absorption band. [b]Emission maximum.

effects of the particle size on the hemolytic behaviors of MSA-QDs on human RBCs, we performed the hemolysis assay by detecting the absorbance of the released hemoglobin from hemolytic RBCs using UV-vis spectrometer. Since the absorption of the three MSA-QDs was in the range of the hemoglobin, the absorption spectrum of the corresponding MSA-QDs at the same concentration to the samples were determined and subtracted from the sample absorption spectrum. The results are shown in Figure 1. The absorbance of the released hemoglobin from the green-, yellow-, and red-emitting MSA-QDs treating RBCs increased in turn, indicating that the larger MSA-QDs exhibited higher hemolytic activity than the smaller ones. The trend is similar to that of recently reported mesoporous silica nanoparticles regarding size.[3] Up to 63.36% hemolysis was determined for the red-emitting MSA-QDs treating RBCs at 500 μg mL^{-1}, while yellow-emitting MSA-QDs only resulted in 7% hemolysis. The green-emitting MSA-QDs even showed a good hemocompatibility, since only 0.14% hemolysis was determined at 500 μg mL^{-1}.

For identifying the effects of the released Cd^{2+} ion and ligand, we estimated their amounts in the samples after incubating with RBCs for 3 h. The Cd^{2+} concentration was determined by differential pulse anodic stripping voltammetry (DPASV). The peak currents were linear with the Cd^{2+} concentrations (see Figure S1 in the Supporting Information). After calculation, the concentrations of the released Cd^{2+} were 12.63, 6.26, and 13.56 μg mL^{-1} in green-, yellow-, and red-emitting QDs treating RBCs samples, respectively. We estimated the hemolytic activity of Cd^{2+} at different concentrations, and found that Cd^{2+} would not induce obvious hemolysis, even when the concentration was up to 100 μg mL^{-1} (Figure S3A in the Supporting Information). Alternatively, we also detected the amounts of released MSA in RBCs treated by MSA-QDs with different sizes using Ellman's test, which is a standard method for the determination of free thiol (Figure S2 in the Supporting Information). The calculated concentrations of MSA in all three samples were <0.5 mM. The hemolytic activity of MSA with different concentrations were also evaluated by using UV-vis spectroscopy (Figure S3B in the
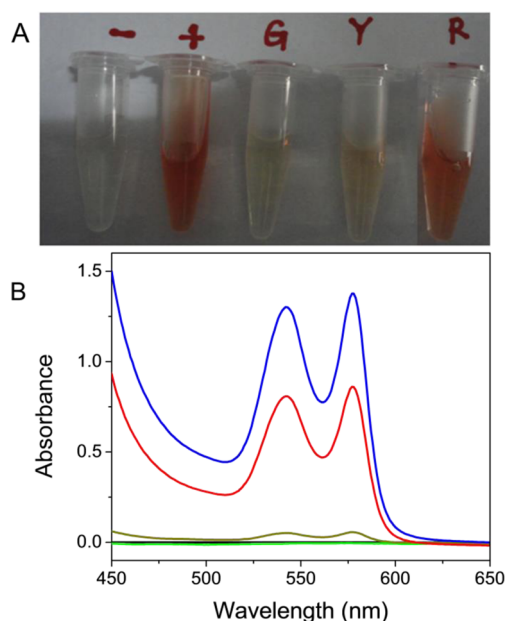

Figure 1. Hemolysis assay for size-dependent MSA-QDs, using water as a positive control (+, blue line) and PBS as a negative control (−, black line). 500 μg mL^{-1} of the green-emitting (G, green line), yellow-emitting (Y, dark yellow line), and red-emitting (R, red line) MSA-QDs were incubated with RBCs for 3 h and the mixtures were centrifuged to detect the presence of hemoglobin in the supernatant visually (A) and the absorption at 542 nm (B) with absorbance at 650 nm as reference.

Supporting Information), which indicates the good hemocompatibility of MSA at <2 mM. These results excluded the effects of released Cd^{2+} and MSA on the hemolytic activity of MSA-QDs with different sizes.

3.2. Observation of Morphological Changes of RBCs by Confocal Microscopy. Figure 2 shows the confocal images of RBCs that were treated with different MSA-QDs for 3 h. In comparison with the control RBCs (Figure 2A), the hemagglutination was induced by exposure of RBCs to the green-emitting MSA-QDs. Most of the RBCs aggregated
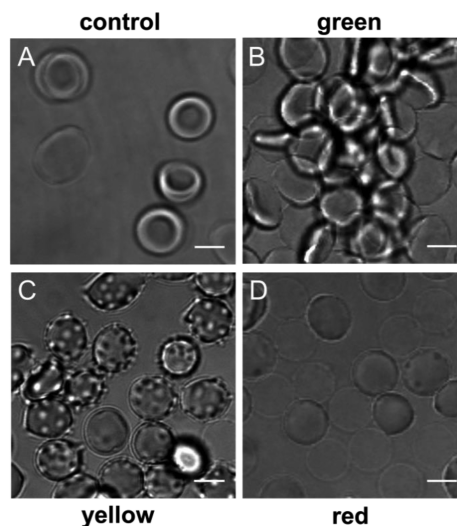

Figure 2. Confocal images of RBCs incubated with (A) PBS, (B) the green-emitting, (C) yellow-emitting, and (D) red-emitting MSA-QDs at a concentration of 500 μg mL^{-1} for 3 h. Scale bar = 10 μm.

together without serious destructive effect (Figure 2B). Unlike the green-emitting MSA-QDs, the yellow-emitting ones caused stomatocytes and echinocytes (Figure 2C). In accordance with the result of the hemolysis assay, many ghost cells were observed after RBCs being incubated with the red-emitting MSA-QDs. Except the ghost cells, some other aberrant cells were also observed (Figure 2D). Several grooves appeared on the surface of RBCs, as reported observation when exposing RBCs to Ag NPs.[1] The formation of these pits might be the outset of membrane damage that would result in pores. As a control experiment, we also estimated the effects of released Cd^{2+} ion and MSA on the shape of RBCs, and found that both of the released Cd^{2+} ion and MSA would not change RBCs morphology (Figure S4 in the Supporting Information). Zhao et al. have attributed the particle-induced hemolysis of RBCs to the membrane deformation, leading to an echinocytic shape transformation.[3] The inability to maintain their normal shape will ultimately lead to the destruction of these cells and result in heavy hemolysis.[3] However, according to our study, the shape transformation is not the main reason that induces the severe hemolysis since the yellow-emitting MSA-QDs only resulted in 7% hemolysis although they also induced an echinocytic shape transformation. This suggests an underlying hemolysis mechanism in addition to the formation of echinocytic shape.

3.3. Structural Changes of RBCs Membranes. For revealing the underlying toxic mechanism of MSA-QDs in RBCs regarding size, we measured the ATR−FT-IR spectra of the corresponding RBCs in accordance with Figure 2. Figure 3A shows the FT-IR spectra of RBCs incubated with PBS (black), green-emitting (green), yellow-emitting (dark yellow) and red-emitting (red) MSA-QDs for 3 h in the CH stretching region. The bands at 2852 and 2928 cm^{-1} are assigned to the symmetric (ν_s) and asymmetric (ν_{as}) CH_2 stretching mode of the methylene chains in membrane lipids. The bands at 2871 and 2958 cm^{-1} come from the symmetric and asymmetric

stretching mode of the CH_3 groups in membrane lipids and proteins.[24,35] Upon the reaction of MSA-QDs, the green- and yellow-emitting MSA-QDs only induced slight blue-shift of the $\nu_s(CH_3)$ to 2873 cm^{-1}, while the red-emitting MSA-QDs induced the blue-shift of the $\nu_s(CH_2)$ and $\nu_{as}(CH_2)$ to 2857 and 2930 cm^{-1} in addition to the blue-shift of the $\nu_s(CH_3)$. This indicates that the red-emitting MSA-QDs have a profound effect on the conformation of RBCs lipid. Figure 3B shows the corresponding FT-IR spectra in the fingerprint region from 1800 cm^{-1} to 1000 cm^{-1}. The spectra between 1480 cm^{-1} and 1700 cm^{-1} were divided by 3 in order to improve the resolution from 1480 cm^{-1} to 1000 cm^{-1}. In the spectra of control RBCs (black), the band at 1734 and 1718 cm^{-1} are attributed to the $\nu(C{=}O)$ of phospholipids, cholesterol esters, and glycerides of RBC membranes.[22] After treating cells with the green- and yellow-emitting MSA-QDs, these peaks were significantly affected, while they were not affected after treating cells with the red-emitting MSA-QDs. These results indicate that smaller green- and yellow-emitting, but not red-emitting QDs had strong interaction with carbonyl groups of the RBCs membranes. The bands at 1367 and 1341 cm^{-1} are from the wagging vibration of methylene fragments in the kink and end-gauche conformations of RBC membrane.[38] After the cells being treated with the three MSA-QDs, only the red-emitting QDs led to the disappearance of the peak at 1367 cm^{-1} and intensive band at 1341 cm^{-1}, suggesting a bigger disturbance in the conformers of lipid. The bands in the region of 1145−1000 cm^{-1} are mainly assigned to the vibration of lipid, polysaccharides, and glucose.[22] The bands at 1127 and 1055 cm^{-1} have been assigned to C−O stretching vibration $\nu(C{-}O)$ in glucose, lactic acid, and polysaccharides.[22,39] It is obviously seen that the interaction of the green- and yellow-emitting MSA-QDs, especially the green-emitting MSA-QDs resulted in apparent decrease of the two peaks in their intensity, suggesting the strong interaction of smaller green- and yellow-emitting MSA-QDs with glycocalyx. The band at 1090 cm^{-1} has been assigned to symmetric vibration of PO_2^-, $\nu_s(PO_2^-)$, coupled with C−O stretching in sugar.[22] Here, we preferred to assign this peak mainly to the $\nu_s(PO_2^-)$ since the peak position was consistent with that observed at the model membranes (Figure 4A). The peak shifted to lower wavenumber after treating cells with the three MSA-QDs, which might be caused by the formation of hydrogen bonds between MSA-QDs and phosphate groups of the lipid. It is worth noting that only the interaction of the red-emitting MSA-QDs resulted in a new peak at 1013 cm^{-1} and intensive band at 1150 cm^{-1} (Figure 3B). It has been reported that the coordination of the phosphate O atom with titanium on the surface of titania nanoparticles resulted in the similar peaks at ~1150 and 1004 cm^{-1}, and red-shift of the $\nu_s(PO_2^-)$, assigned to the three P−O stretching modes of phosphate-titanium complex.[40,41] Therefore, we deduced that the interaction of the red-emitting MSA-QDs with RBCs membrane might also form the phosphate−cadmium complex. Meanwhile, we also observed an intensive peak at 1107 cm^{-1} after the red- and yellow-emitting (especially the red-emitting) MSA-QDs interacting with RBCs, which has been assigned to asymmetric stretching vibration of PO_3^{2-}, $\nu_{as}(PO_3^{2-})$.[42] This suggests that part of the phosphate ester bonds were broken to form terminal phosphoryl groups due to the interaction of the red-emitting MSA-QDs. This might cause the pore formation of lipid membrane of RBCs and subsequent hemolysis. The strong effect of the red-emitting MSA-QDs on
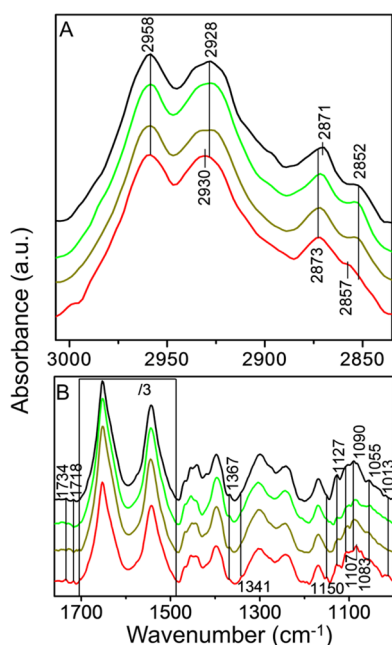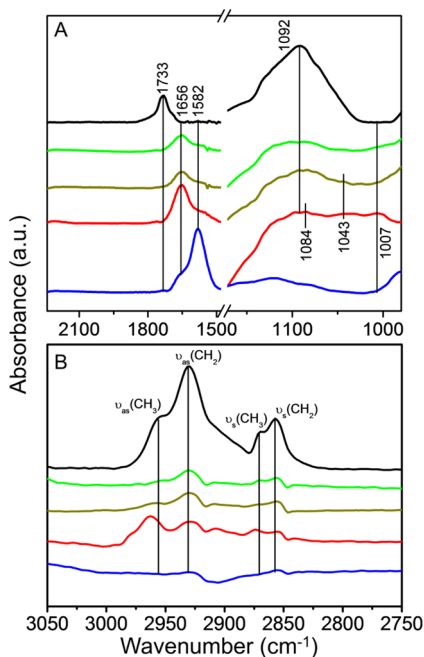

Figure 3. FT-IR spectra of RBCs (A) at the CH stretching region and (B) at the fingerprint region after incubating with PBS (black) as a control, and 500 μg mL^{-1} MSA-QDs with emitting color of green (green), yellow (dark yellow), and red (red) for 3 h.

Figure 4. (A) SEIRAS of vesicles containing the lipids of RBCs membrane adsorbed on the DT-modified gold surface (black), the lipid/DT modified gold surface treated by green-emitting (green), yellow-emitting (dark yellow), red-emitting (red) MSA-QDs, and MSA-QDs adsorbed on the gold surface (blue). (B) SEIRAS at CH stretching region of the lipid, MSA-QDs-adsorbed lipid, and control MSA-QDs as stated in panel A.

the lipid membrane should also induce a bigger disturbance in the conformation of lipid as discussed above.

To further strengthen the evidence that the red-emitting MSA-QDs-induced damage to the RBCs lipid and eliminate the disturbance of other components in this region, we measured the vibrations of MSA-QDs-treated model membranes formed on solid support by surface-enhanced FT-IR spectroscopy. Vesicles with the lipid contents as similar as that in RBCs membranes were fused on a solid support by the hydrophobic interaction between the vesicles and the hydrophobic surface of a self-assembled monolayer of DT preadsorbed on a gold film.[24] The surface-enhanced FT-IR absorption spectrum (SEIRAS) of the model membrane in the region of 1000−2000 cm^{-1} is shown in Figure 4A (black), taking the DT-modified Au surface immersed in aqueous solution as reference. The typical band at 1733 cm^{-1} due to the C=O stretching vibration of the lipid indicates the formation of the model membrane by vesicle fusion. The band at 1092 cm^{-1} is from ν_s (PO$_2^-$). To study the effects of MAS-QDs on lipid membrane, the SEIRAS of lipid membrane exposed to MSA-QDs regarding size was recorded. A broad peak at 1656 cm^{-1} was observed after the lipid membrane being exposed to the three MSA-QDs. In comparison with the SEIRAS of the control MSA-QDs, which shows a strong peak at 1582 cm^{-1} and two shoulder peaks at 1656 and 1733 cm^{-1} assigned to asymmetric stretching of COO$^-$ and symmetric stretching of C=O,[43] the broad peak at 1656 cm^{-1} should be assigned to the ν_s(C=O) of protonated carboxylic acid coupled with OH bending vibration of water. This suggests that the free COO$^-$ groups of the MSA-QDs may participate in hydrogen bonding when QDs interact with lipid membrane, irrespective of size. However, the spectra changes at the region of 1000−1200 cm^{-1} are apparently

different. The spectra in this region should come from the weak absorption of adsorbed MSA-QDs (control QDs) and the enhanced phosphate vibration due to the formation of an inner-sphere complex with nanoparticles. If they mainly came from the adsorbed MSA-QDs, they should have spectra similar to that of the adsorbed MSA-QDs in the region of 1400−1800 cm^{-1}, irrespective of size. Therefore, the difference in the spectra should mainly come from different vibrational changes of the phosphate-ester bond due to the reaction of different MSA-QDs. Exposure of the three MSA-QDs, especially the red-emitting MSA-QDs, resulted in an apparent red-shift of the maximum peak to 1084 cm^{-1}, indicating their interactions with phosphate group of the lipid. Besides, the interaction of the red-emitting MSA-QDs also induced a new peak at 1007 cm^{-1}, because of the ν_s(P−O) of coordinated phosphate groups.[41] Meanwhile, we also observed a peak at 1043 cm^{-1} after the yellow- and red-emitting MSA-QDs interacting with model membranes. Especially for the red-emitting MSA-QDs, we observed a broad peak at ∼1043 cm^{-1} after their interaction, which has been assigned to symmetric stretching vibration of PO$_3^{2-}$, ν_s(PO$_3^{2-}$). These results indicate that the red-emitting MSA-QDs induced most serious damage to the phosphate-ester bond of lipid. Some of phosphate ester bonds were broken to form terminal phosphoryl groups.

Figure 4B shows the SEIRAS at CH stretching region. Interaction of the green- and yellow-emitting MSA-QDs induced a strong absorption at the position of ν_s(CH$_2$) and ν_{as}(CH$_2$) and a weak absorption at the position of ν_s(CH$_3$) and ν_{as}(CH$_3$). In stark contrast, interaction of the red-emitting MSA-QDs induced a strong ν_{as}(CH$_3$) and ν_s(CH$_3$) absorption at higher wavenumber, in addition to the absorption at the position of ν_s(CH$_2$) and ν_{as}(CH$_2$). Since the SEIRAS of control MSA-QDs also shows strong absorption at the position of ν_s(CH$_2$) and ν_{as}(CH$_2$), it is difficult to judge the spectroscopic character in these two positions. However, the MSA-QDs-induced ν_{as}(CH$_3$) and ν_s(CH$_3$) vibrations that were not existent in the SEIRAS of control MSA-QDs should reflect the interaction between QDs and CH$_3$ groups of lipid. The free COO$^-$ group on the surface of MSA-QDs may form a hydrogen bond with the H atom of the CH$_3$ groups of lipid. Obviously, bigger red-emitting MSA-QDs have the strongest ability to form hydrogen bonds with the H atoms of lipids.

The amide I band of protein often reflects quantitative and qualitative relationships between the various secondary structures in protein.[21,44,45] The proteins of RBCs are mainly composed of ∼90% hemoglobin and ∼10% spectrin, which is a skeletal membrane protein.[22] For analyzing the variety of the secondary structure quantitatively, we decomposed the amide I band by Gaussian curve-fitting, as shown in Figure 5A. The main band centered at 1652 cm^{-1} has been assigned to the α-helix, the bands at 1620−1637 cm^{-1} are attributed to β-sheet, and the bands at 1673−1684 cm^{-1} are attributed to β-turn, respectively.[46] The proteins in the control RBCs have ∼70% α-helix, ∼19% β-sheet, and ∼11% β-turn (Figure 5B). After incubating RBCs with the green- and yellow-emitting MSA-QDs for 3 h, the content of α-helix was sequentially decreased with the increase of the β-sheet structure. However, incubating with the red-emitting MSA-QDs resulted in slight increase of α-helix and decrease of β-sheet, in comparison to the protein secondary structure in yellow-emitting QDs treated RBCs. However, overall, the contents of α-helix and β-sheet are still different from the contents of protein secondary structure in the control RBCs. The structural changes of the proteins in the
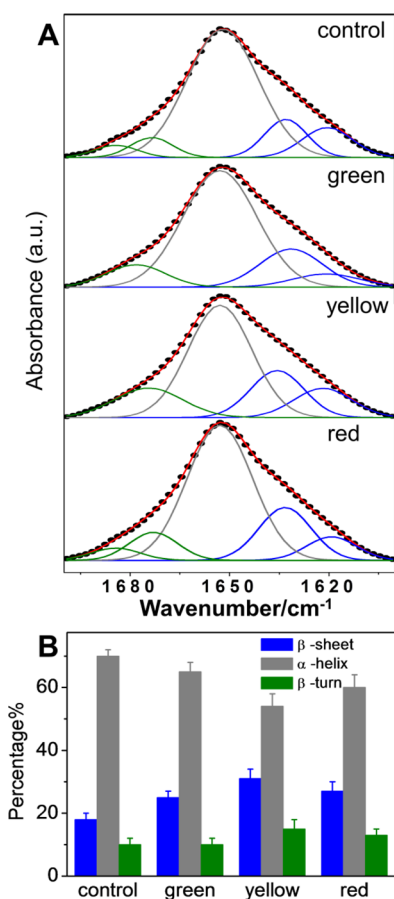
Figure 5. (A) Curve-fitting spectra of the amide I band of proteins in RBCs after being treated with PBS as a control and MSA-QDs with emitting color of green (green), yellow (yellow), and red (red) for 3 h fitted with Gaussian curves. (B) Fraction of the protein secondary structure as determined by quantitative curve-fitting analysis. The value was obtained from two or three experiments; error bars indicate standard deviations from the mean.

cells might be one of the reasons that caused the RBCs shape changes. We also detected the ATP content in RBCs after being treated with MSA-QDs for 3 h (Figure S5 in the Supporting Information). Treating RBCs with the yellow-emitting MSA-QDs resulted in the significant decrease of the ATP content, which might be one of the reasons that caused the shape transformation of RBCs, however the contribution of the red-emitting MSA-QDs-induced decrease in the ATP content was difficult to identify, since it might result from the hemolysis-induced leakage, together with hemoglobin.

As shown in Scheme 1, during the interaction of MSA-QDs with RBCs, the hydrogen bond between the free COO^- groups at the surface of MSA-QDs and the lipid membrane might be formed, irrespective of size. When smaller green- and yellow-emitting MSA-QDs (especially the green-emitting MSA-QDs) approach the RBCs, most of them may have a strong interaction with glycocalyx by forming hydrogen bonds, and part of them may enter the gaps between the long biopolymer chains and interact with outer membrane proteins. For bigger red-emitting QDs, most of them may escape from the capture of glycocalyx and interact with the lipid. They have the strongest ability to form hydrogen bonds with lipids and cause a bigger disturbance in the conformers of lipids. Besides, they break the phosphate ester bond to form a terminal phosphoryl

Scheme 1. Schematic of Possible Interaction of MSA-QDs with RBC Membrane
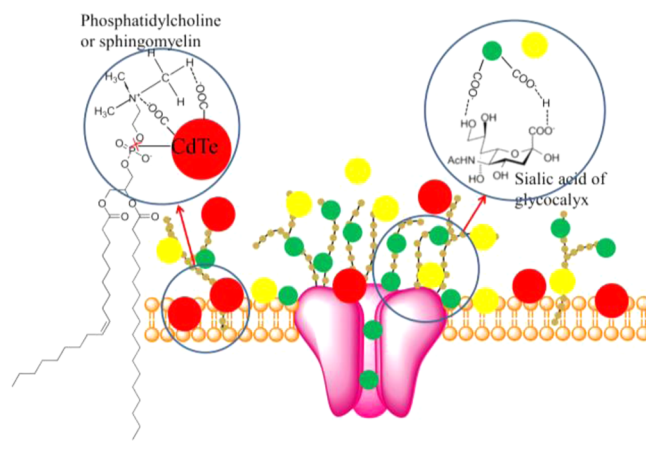
group and a phosphate—cadmium complex, which might cause the pore formation in lipid membrane of RBCs and subsequent hemolysis. The difference in the interaction models for smaller and bigger MSA-QDs might come from the difference in their surface energy regarding size.

4. CONCLUSIONS

This study demonstrated that the nanoparticles of different sizes would induce different red blood cell (RBC) toxicity. The green-emitting QDs induced hemagglutination. The yellow-emitting QDs induced slight hemolysis, although many stomatocytes and echinocytes were formed. The red-emitting QDs induced heavy hemolysis and the formation of many ghost cells. The structural changes in the RBCs were detected by Fourier transform infrared (FT-IR) spectroscopy to further understand the hemolysis mechanism. The results indicated that the MSA-QDs interacted with RBCs via hydrogen bonding, irrespective of size. The green- and yellow-emitting QDs had strong interactions with cellular glycocalyx, while the red-emitting QDs broke the phosphate ester bond and caused bigger changes of lipid conformation. The secondary structure transformation of proteins in RBCs after incubation with MSA-QDs might be related to shape changes in the RBCs. The hemolysis most probably depends on the damage to the phosphate ester bond of lipid. To some extent, our results provide the molecular basis for the hemolysis mechanism for the first time.

■ ASSOCIATED CONTENT

Ⓢ Supporting Information

Detection of the released Cd^{2+} ion and ligand from the QDs and their effects on the RBCs hemolysis, images of RBCs after being treated by PBS, Cd^{2+}, and MSA ligand, and ATP measurement results. This material is available free of charge via the Internet at http://pubs.acs.org.

■ AUTHOR INFORMATION

Corresponding Author
*Tel.: +86 431 85262426. Fax: +86 431 85685653. E-mail address: jiangxiue@ciac.ac.cn.

Notes

The authors declare no competing financial interest.

■ REFERENCES

(1) Asharani, P. V.; Sethu, S.; Vadukumpully, S.; Zhong, S.; Lim, C. T.; Hande, M. P.; Valiyaveettil, S. Investigations on the Structural Damage in Human Erythrocytes Exposed to Silver, Gold, and Platinum Nanoparticles. *Adv. Funct. Mater.* **2010**, *20*, 1233−1242.

(2) Yu, T.; Malugin, A.; Ghandehari, H. Impact of Silica Nanoparticle Design on Cellular Toxicity and Hemolytic Activity. *ACS Nano* **2011**, *5*, 5717−5728.

(3) Zhao, Y.; Sun, X.; Zhang, G.; Trewyn, B. G.; Slowing, I. I.; Lin, V. S.-Y. Interaction of Mesoporous Silica Nanoparticles with Human Red Blood Cell Membranes: Size and Surface Effects. *ACS Nano* **2011**, *5*, 1366−1375.

(4) Choi, J.; Reipa, V.; Hitchins, V. M.; Goering, P. L.; Malinauskas, R. A. Physicochemical Characterization and In Vitro Hemolysis Evaluation of Silver Nanoparticles. *Toxicol. Sci.* **2011**, *123*, 133−143.

(5) Lin, Y.-S.; Haynes, C. L. Impacts of Mesoporous Silica Nanoparticle Size, Pore Ordering, and Pore Integrity on Hemolytic Activity. *J. Am. Chem. Soc.* **2010**, *132*, 4834−4842.

(6) Shi, J.; Hedberg, Y.; Lundin, M.; Odnevall Wallinder, I.; Karlsson, H. L.; Möller, L. Hemolytic Properties of Synthetic Nano- and Porous Silica Particles: The Effect of Surface Properties and the Protection by the Plasma Corona. *Acta Biomater.* **2012**, *8*, 3478−3490.

(7) Backman, L. Shape Control in the Human Red Cell. *J. Cell Sci.* **1986**, *80*, 281−298.

(8) Nakao, M.; Nakao, T.; Yamazoe, S. Adenosine Triphosphate and Maintenance of Shape of the Human Red Cells. *Nature* **1960**, *187*, 945−946.

(9) Nakao, M.; Yamazoe, S.; Yoshikawa, H.; Nakao, T. Adenosine Triphosphate and Shape of Erythrocytes. *J. Biochem.* **1961**, *49*, 487−492.

(10) LaBrake, C. C.; Wang, L.; Keiderling, T. A.; Fung, L. W. M. Fourier Transform Infrared Spectroscopic Studies of the Secondary Structure of Spectrin under Different Ionic Strengths. *Biochemistry* **1993**, *32*, 10296−10302.

(11) Park, Y. K.; Best, C. A.; Auth, T.; Gov, N. S.; Safran, S. A.; Popescu, G.; Suresh, S.; Feld, M. S. Metabolic Remodeling of the Human Red Blood Cell Membrane. *Proc. Natl. Acad. Sci. U. S. A* **2010**, *107*, 1289−1294.

(12) Liu, X.; Huang, H.; Liu, G.; Zhou, W.; Chen, Y.; Jin, Q.; Ji, J. Multidentate Zwitterionic Chitosan Oligosaccharide Modified Gold Nanoparticles: Stability, Biocompatibility and Cell Interactions. *Nanoscale* **2013**, *5*, 3982−3991.

(13) Slowing, I. I.; Wu, C.-W.; Vivero-Escoto, J. L.; Lin, V. S. Y. Mesoporous Silica Nanoparticles for Reducing Hemolytic Activity Towards Mammalian Red Blood Cells. *Small* **2009**, *5*, 57−62.

(14) Sovadinova, I.; Palermo, E. F.; Huang, R.; Thoma, L. M.; Kuroda, K. Mechanism of Polymer-Induced Hemolysis: Nanosized Pore Formation and Osmotic Lysis. *Biomacromolecules* **2011**, *12*, 260−268.

(15) Chen, H.-C.; Mendelsohn, R.; Rerek, M. E.; Moore, D. J. Fourier Transform Infrared Spectroscopy and Differential Scanning Calorimetry Studies of Fatty Acid Homogeneous Ceramide 2. *Biochim. Biophys. Acta, Biomembr.* **2000**, *1468*, 293−303.

(16) Mantsch, H. H.; McElhaney, R. N. Phospholipid Phase Transitions in Model and Biological Membranes as Studied by Infrared Spectroscopy. *Chem. Phys. Lipids* **1991**, *57*, 213−226.

(17) Mendelsohn, R.; Moore, D. J. Vibrational Spectroscopic Studies of Lipid Domains in Biomembranes and Model Systems. *Chem. Phys. Lipids* **1998**, *96*, 141−157.

(18) Moore, D. J.; Gioioso, S.; Sills, R. H.; Mendelsohn, R. Some Relationships between Membrane Phospholipid Domains, Conforma-tional Order, and Cell Shape in Intact Human Erythrocytes. *Biochim. Biophys. Acta, Biomembr.* **1999**, *1415*, 342−348.

(19) Derenne, A.; Verdonck, M.; Goormaghtigh, E. The Effect of Anticancer Drugs on Seven Cell Lines Monitored by FT-IR Spectroscopy. *Analyst* **2012**, *137*, 3255−3264.

(20) Jiang, W.; Saxena, A.; Song, B.; Ward, B. B.; Beveridge, T. J.; Myneni, S. C. B. Elucidation of Functional Groups on Gram-Positive and Gram-Negative Bacterial Surfaces Using Infrared Spectroscopy. *Langmuir* **2004**, *20*, 11433−11442.

(21) Jiang, W.; Yang, K.; Vachet, R. W.; Xing, B. S. Interaction between Oxide Nanoparticles and Biomolecules of the Bacterial Cell Envelope As Examined by Infrared Spectroscopy. *Langmuir* **2010**, *26*, 18071−18077.

(22) Petibois, C.; Deleris, G. Evidence that Erythrocytes are Highly Susceptible to Exercise Oxidative Stress: FT-IR Spectrometric Studies at the Molecular Level. *Cell Biol. Int.* **2005**, *29*, 709−716.

(23) Rigas, B.; Morgello, S.; Goldman, I. S.; Wong, P. T. Human Colorectal Cancers Display Abnormal Fourier-Transform Infrared Spectra. *Proc. Natl. Acad. Sci. U. S. A.* **1990**, *87*, 8140−8144.

(24) Wang, T.; Bai, J.; Jiang, X.; Nienhaus, G. U. Cellular Uptake of Nanoparticles by Membrane Penetration: A Study Combining Confocal Microscopy with FT-IR Spectroelectrochemistry. *ACS Nano* **2012**, *6*, 1251−1259.

(25) Howarth, M.; Takao, K.; Hayashi, Y.; Ting, A. Y. Targeting Quantum Dots to Surface Proteins in Living Cells with Biotin Ligase. *Proc. Natl. Acad. Sci. U. S. A.* **2005**, *102*, 7583−7588.

(26) Klostranec, J. M.; Chan, W. C. W. Quantum Dots in Biological and Biomedical Research: Recent Progress and Present Challenges. *Adv. Mater.* **2006**, *18*, 1953−1964.

(27) Larson, D. R.; Zipfel, W. R.; Williams, R. M.; Clark, S. W.; Bruchez, M. P.; Wise, F. W.; Webb, W. W. Water-Soluble Quantum Dots for Multiphoton Fluorescence Imaging In Vivo. *Science* **2003**, *300*, 1434−1436.

(28) Clift, M. J. D.; Rothen-Rutishauser, B.; Brown, D. M.; Duffin, R.; Donaldson, K.; Proudfoot, L.; Guy, K.; Stone, V. The Impact of Different Nanoparticle Surface Chemistry and Size on Uptake and Toxicity in a Murine Macrophage Cell Line. *Toxicol. Appl. Pharmacol.* **2008**, *232*, 418−427.

(29) Fahmi, M. Z.; Chang, J.-Y. Forming Double Layer-Encapsulated Quantum Dots for Bio-Imaging and Cell Targeting. *Nanoscale* **2013**, *5*, 1517−1528.

(30) Kirchner, C.; Liedl, T.; Kudera, S.; Pellegrino, T.; Javier, A. M.; Gaub, H. E.; Stolzle, S.; Fertig, N.; Parak, W. J. Cytotoxicity of Colloidal CdSe and CdSe/ZnS Nanoparticles. *Nano Lett.* **2005**, *5*, 331−338.

(31) Liu, Y. F.; Xie, B.; Yin, Z. G.; Fang, S. M.; Zhao, J. B. Synthesis of Highly Stable CdTe/CdS Quantum Dots with Biocompatibility. *Eur. J. Inorg. Chem.* **2010**, *2010*, 1501−1506.

(32) Bao, H.; Wang, E.; Dong, S. One-Pot Synthesis of CdTe Nanocrystals and Shape Control of Luminescent CdTe−Cystine Nanocomposites. *Small* **2006**, *2*, 476−480.

(33) Ying, E.; Li, D.; Guo, S.; Dong, S.; Wang, J. Synthesis and Bio-Imaging Application of Highly Luminescent Mercaptosuccinic Acid-Coated CdTe Nanocrystals. *PLoS One* **2008**, *3*, e2222.

(34) Röcker, C.; Pötzl, M.; Zhang, F.; Parak, W. J.; Nienhaus, G. U. A Quantitative Fluorescence Study of Protein Monolayer Formation on Colloidal Nanoparticles. *Nat. Nanotechnol.* **2009**, *4*, 577−580.

(35) Ataka, K.; Giess, F.; Knoll, W.; Naumann, R.; Haber-Pohlmeier, S.; Richter, B.; Heberle, J. Oriented Attachment and Membrane Reconstitution of His-Tagged Cytochrome c Oxidase to a Gold Electrode: In Situ Monitoring by Surface-Enhanced Infrared Absorption Spectroscopy. *J. Am. Chem. Soc.* **2004**, *126*, 16199−16206.

(36) Ataka, K.; Heberle, J. Electrochemically Induced Surface-Enhanced Infrared Difference Absorption (SEIDA) Spectroscopy of a Protein Monolayer. *J. Am. Chem. Soc.* **2003**, *125*, 4986−4987.

(37) Ataka, K.; Heberle, J. Functional Vibrational Spectroscopy of a Cytochrome c Monolayer: SEIDAS Probes the Interaction with Different Surface-Modified Electrodes. *J. Am. Chem. Soc.* **2004**, *126*, 9445−9457.

(38) Rozner, S.; Shalev, D. E.; Shames, A. I.; Ottaviani, M. F.; Aserin, A.; Garti, N. Do Food Microemulsions and Dietary Mixed Micelles Interact? *Colloids Surf., B* **2010**, *77*, 22−30.

(39) Petibois, C.; Melin, A.-M.; Perromat, A.; Cazorla, G.; Déléris, G. Glucose and Lactate Concentration Determination on Single Micro-samples by Fourier-Transform Infrared Spectroscopy. *J. Lab. Clin. Med.* **2000**, *135*, 210−215.

(40) Connor, P. A.; McQuillan, A. J. Phosphate Adsorption onto TiO$_2$ from Aqueous Solutions: An in Situ Internal Reflection Infrared Spectroscopic Study. *Langmuir* **1999**, *15*, 2916−2921.

(41) Petrone, L.; Easingwood, R.; Barker, M. F.; McQuillan, A. J. In situ ATR-IR Spectroscopic and Electron Microscopic Analyses of Settlement Secretions of Undaria Pinnatifida Kelp Spores. *J. R. Soc., Interface* **2011**, *8*, 410−422.

(42) Parikh, S. J.; Chorover, J. ATR-FT-IR Spectroscopy Reveals Bond Formation During Bacterial Adhesion to Iron Oxide. *Langmuir* **2006**, *22*, 8492−8500.

(43) Ibrahim, M.; Nada, A.; Kamal, D. E. Density Functional Theory and FT-IR Spectroscopic Study of Carboxyl Group. *Indian J. Pure Appl. Phys.* **2005**, *43*, 911−917.

(44) Torii, H.; Tasumi, M. In *Infrared Spectroscopy of Biomolecules*; Mantsch, H. H., Chapman, D., Eds.; John Wiley & Sons: New York; 1996; pp 1−18.

(45) Naumann, D.; Schultz, C. P.; Helm, D. In *Infrared Spectroscopy of Biomolecules*; Mantsch, H. H., Chapman, D., Eds.; John Wiley & Sons: New York; 1996; pp 279−310.

(46) Kong, J.; Yu, S. Fourier Transform Infrared Spectroscopic Analysis of Protein Secondary Structures. *Acta Biochim. Biophys. Sin.* **2007**, *39*, 549−559.